

DOI: 10.1002/ ((please add manuscript number))

**Article type: Full Paper**

**Photoactivity and Stability Co-enhancement: When Localized Plasmons Meet Oxygen Vacancies in MgO**

*Zhengqing Liu,<sup>+</sup> Ziyang Lu,<sup>+</sup> Michel Bosman, Na Li, Terry J. Frankcombe,<sup>\*</sup> Guohua Jia, Antonio Tricoli, Yun Liu, Yaping Du,<sup>\*</sup> and Zongyou Yin<sup>\*</sup>*

Z. Q. Liu,<sup>[+]</sup> Prof. Y. P. Du

School of Materials Science and Engineering, National Institute for Advanced Materials,  
Center for Rare Earth and Inorganic Functional Materials  
Nankai University  
Tianjin 300350 (P.R. China)  
E-mail: ypdu@nankai.edu.cn

Z. Y. Lu,<sup>[+]</sup> Prof. Z. Y. Yin, Prof. Y. Liu

Research School of Chemistry  
The Australian National University  
Canberra, Australian Capital Territory 2601, Australia  
E-mail: zongyou.yin@anu.edu.au

M. Bosman

Department of Materials Science and Engineering  
National University of Singapore  
9 Engineering Drive 1, 117575, Singapore

N. Li

Frontier Institute of Science and Technology  
Xi'an Jiaotong University,  
Xi'an 710049 (P.R. China)

Prof. T. J. Frankcombe

School of Physical, Environmental and Mathematical Sciences  
University of New South Wales  
Canberra, ACT 2600, Australia.  
E-mail: t.frankcombe@adfa.edu.au

G. H. Jia

Nanochemistry Research Institute, Department of Chemistry  
Curtin University  
Perth, Western Australia 6102, Australia.

A. Tricoli

Research School of Engineering  
The Australian National University  
Canberra, Australian Capital Territory 2601, Australia

<sup>[+]</sup>These authors contributed equally to this work.

**Keywords:** Plasmonic defect nanosystems, oxygen vacancies, surface plasmon, co-enhancement of photoactivity and stability

**Abstract text:** Durability is still one of the key obstacles for the further development of photocatalytic energy-conversion systems, especially low-dimensional ones. Encouragingly, recent studies show that nano insulators such as SiO<sub>2</sub> and MgO exhibit substantially enhanced photocatalytic durability than the typical semiconductor p25 TiO<sub>2</sub>. Extending this knowledge, we developed MgO-Au plasmonic defect nanosystems that combine the stable photoactivity from MgO surface defects with energy-focusing plasmonics from Au nanoparticles (NPs), where Au NPs were anchored onto monodisperse MgO nanotemplates. Theoretical calculations revealed that the mid-gap defect (MGD) states in MgO were generated by oxygen vacancies, which provide the main avenues for upward electron transitions under photoexcitation. These electrons drive stable proton photoreduction to H<sub>2</sub> gas via water splitting. We demonstrate a synergistic interaction between Au's localized plasmons and MgO's oxygen vacancies, which enhances MgO's photoactivity and stability simultaneously. Such co-enhancement is attributed to the stable longitudinal-plasmon-free Au NPs, which provide robust hot electrons capable of overcoming the interband transition barrier (~1.8 eV) to reach proton reduction potential for H<sub>2</sub> generation. The demonstrated plasmonic defect nanosystems are expected to open a new avenue for developing highly enduring photoredox systems for the integration of multi-functionalities in energy conversion, environmental decontamination and climate change mitigation.

## 1. Introduction

Localized Surface Plasmon Resonances (LSPRs) are collective oscillations of the free electrons near the vicinity of metal nanostructures (e.g., Au, Ag, Al and Cu), and have been widely researched for their applications in bio-/chemical sensing,<sup>[1-4]</sup> energy conversion,<sup>[5-10]</sup>

environmental decontamination,<sup>[11-15]</sup> plasmon-polariton coupling,<sup>[16-18]</sup> single-molecular coupling<sup>[19]</sup> and quantum plasmon resonances,<sup>[20]</sup> etc. In this work, we will focus on photocatalysis, an emerging application field for plasmonics. Generally, by introducing LSPRs into a photocatalytic system, light energy is concentrated into nanoscale volumes, so we expect improved cost-effectiveness. In other words, the increase of the functional performance is expected to outweigh the cost increase brought by LSPR-nanomaterials such as Au and Ag. To achieve this, a fine chemical synthesis strategy is required to controllably anchor on-demand LSPR-nanomaterials onto the surface of photocatalytic templates. Furthermore, accurate understanding of the local LSPR behavior of nanoparticles (NPs) is an important prerequisite for utilization and maximization of LSPR's functionalities in photocatalysis. Considerable efforts have been made towards coupling Au nanostructures to various semiconductors, such as TiO<sub>2</sub>,<sup>[21]</sup> CdS,<sup>[22]</sup> WO<sub>3</sub>,<sup>[23]</sup> Bi<sub>3</sub>TaO<sub>7</sub>,<sup>[12]</sup> and MoS<sub>2</sub>,<sup>[8]</sup> for promoting water splitting reactions.<sup>[10]</sup> By contrast, LSPRs from Au nanostructures on insulator photocatalysts (e.g., SiO<sub>2</sub>, Al<sub>2</sub>O<sub>3</sub> and MgO) are rarely reported.

Chemical stability is one of the key bottlenecks for further industrialization of photochemical systems. As observed in our previous work,<sup>[24]</sup> even the successful material TiO<sub>2</sub> still meets photochemical stability issues when it is downscaled to the nanoscale for energy conversion. Nanoscale TiO<sub>2</sub> loses its efficacy faster than the insulator photocatalysts SiO<sub>2</sub> and MgO in which functional photocatalysis arises from the photoreduction by the excited electrons at mid-gap defect states which protect insulators from being directly reduced by electrons. By using the synthesis route from our recent work<sup>[24]</sup> as a starting point, we aim to produce MgO in which - by its mesoporous nature - a large part of the surface defects are exposed to the environment. It then becomes interesting to ask the question: can we integrate the durable light-focusing action of Au NPs to further enhance the photocatalytic activity of MgO without degrading its photochemical stability?

Herein, we investigate the effects of interactions between LSPR and defect states on photocatalysis, by anchoring Au NPs onto mesoporous MgO nanocrystals to form the MgO-Au nanocomposites. Our results show that the photocatalysis from non-intrinsic defect electrical states of nanoscale MgO is significantly improved by introducing Au NPs as local surface nanoplasmonic resonators. Importantly, the MgO-Au system exhibits a stable photocatalysis for hydrogen generation from water splitting. By fine characterization on Au's LSPR with monochromated electron energy-loss spectroscopy (EELS) in a scanning transmission electron microscope (STEM), the Au NPs' distinctive size- and shape-dependent local plasmon resonance peaks were observed. The typical plasmon resonances of Au NPs at high energy ( $\sim 2.3$  eV) are consistent with the ultraviolet-visible (UV-Vis) absorption under far-field conditions and contribute most to the photocatalysis enhancement, while the low-energy resonances contribute less. The stable  $H_2$  production of the MgO is associated with non-intrinsic surface electrical states, i.e. the defect energy levels as signified by density functional theory calculations, and the enhanced  $H_2$  production from MgO-Au nanocomposites is associated with Au's local surface nanoplasmonic enhancement on the photocatalysis.

## 2. Results and Discussion

### 2.1. Synthesis and Characterization of MgO-Au Nanocomposites

Monodisperse MgO NPs with mesoporous morphology (Figure S1a,b, Supporting Information) were synthesized by a facile green approach as presented in our recent work.<sup>[24]</sup> The diameter of the as-synthesized mesoporous MgO NPs is about  $84 \pm 11$  nm (Figure S1c, Supporting Information). As described in the Supplement, Au NPs were integrated onto the surface of MgO NPs to form the MgO-Au nanocomposites. The X-ray diffraction (XRD) patterns (**Figure 1a**) show that the MgO component of MgO-Au nanocomposites exists in a single, exclusively face-centered-cubic phase (space group: Fm-3m, JCPDS: 45-0946), which

is consistent with the pure MgO NPs (Figure S2, Supporting Information). Powder X-ray diffraction (PXRD) analysis measures the crystal parameters to be  $a = b = c = 4.211 \text{ \AA}$ , and no diffraction peaks from any other chemical species such as  $\text{Mg}(\text{OH})_2$  or  $\text{MgCO}_3$  are detectable. For Au component of MgO-Au nanocomposites, all of the peaks in the XRD patterns (Figure 1a) matched well with the cubic Au (space group: Fm-3m (225), JCPDS 04-0784). Transmission electron microscopy (TEM) and high-angle annular dark-field (HAADF)-STEM characterization were employed to further investigate the composite of MgO-Au nanocomposites. It can be seen that a large number of Au NPs were loaded on the surface of MgO NPs (Figure 1b,c), the average size of Au NPs is  $12.6 \pm 1.5 \text{ nm}$  (Figure S3, Supporting Information). The observed interplanar distance between the lattice fringes is 0.21 nm in MgO crystal (Figure 1d) and 0.23 nm in Au (Figure 1e), corresponding to the (200) planes of MgO and (111) planes of Au, respectively, confirming the crystalline nature of both components in the MgO-Au nanocomposites.

One common characteristic of MgO and Au is their chemical stability, which is essential for durable operations under strong light illumination and also makes them feasible for oxygen plasma treatments. In order to remove their capping ligands oleylamine (OM) and oleic acid (OA), we employed an oxygen plasma treatment on the dried MgO-Au nanocomposites powders. Encouragingly, the oxygen plasma treatment, a low-cost environment-friendly technique, is very efficient in cleaning the nanomaterial surfaces by removing the organic capping ligands, as demonstrated by the Fourier transform infrared (FTIR) spectra (Figure S4, Supporting Information) and contact angle (Figure S5, Supporting Information). Furthermore, the phase of MgO-Au nanocomposites after plasma treatment was confirmed by XRD pattern (Figure S6, Supporting Information), which was similar to the XRD pattern of the initial MgO-Au nanocomposites (Figure 1a).

**Figure 2** shows the room-temperature UV-Vis absorption and photoluminescence (PL) spectra of MgO-Au nanocomposites and pure MgO NPs as control. All of the colloidal

solutions exhibited continuous absorption across the UV wavelength range. Two broad absorption peaks were obviously observed around 220 nm (5.6 eV) and 270 nm (4.6 eV), which are usually ascribed to be from the excitation of defect states, which belong to O<sup>2-</sup> surface anions on the edge (4-fold coordinated) and on the corner (3-fold coordinated) of the MgO nanocrystal,<sup>[25,26]</sup> respectively. These defect energy levels sit in the band gap of MgO ( $E_{g-MgO} = 7.8$  eV).<sup>[27,28]</sup> For MgO-Au nanocomposites, a new absorption peak at 530 nm appeared and the intensity increased with higher Au loading (Figure 2a and inset). This peak results from the excitation of localized plasmon resonances in the Au NPs, and higher Au NPs loading generates stronger plasmon resonance absorption. Although MgO is a wide band gap insulator, optical transitions in the visible range were observed in our mesoporous MgO NPs. Figure 2b shows PL spectra of pure MgO NPs and MgO-Au nanocomposites at an excitation wavelength of 340 nm. The dominant PL emission centered at ~430 nm, i.e. 2.9 eV, originates from the surface states and the presence of structural defects, such as oxygen vacancies,<sup>[29-31]</sup> to be discussed in more details below. Furthermore, the XPS spectra of O 1s show that oxygen vacancies are present in the as-prepared MgO and MgO-Au samples (Figure S7, Supporting Information). It is worth mentioning here that the intensity of both UV-Vis and PL absorption from the MgO component of MgO-Au nanocomposites decreased with higher Au loading (Figure 2a,b), in stark contrast to the UV-Vis absorption from the Au component itself (inset of Figure 2a).

## 2.2. Monochromated EELS Study of Individual Au NPs on MgO NPs

The optical activity of Au NPs results from their LSPRs, so we used monochromated EELS in a STEM to characterize localized surface plasmons in the Au NPs. The experimental configuration for the EELS plasmon resonance measurements is schematically illustrated in **Figure 3a**. Due to the high spatial resolution of this technique, the EELS spectra can be measured from individual Au NPs on MgO NPs. In our experiments, we used the typical

MgO-Au nanocomposites with loading 23 wt% Au NPs, as determined by inductively coupled plasma atomic emission spectroscopy (ICP-AES) measurements. As seen from the STEM image of Figure 3b, the grey sphere-like structure is MgO and the small, brighter particles are Au NPs, which are grown on the mesoporous MgO NP. Spectra were acquired by placing the electron beam at locations I-VII to investigate the Au size/shape effects (Figure 3b), and the obtained EELS spectra for MgO, Au and MgO-Au nanocomposites are presented in Figure 3c. Spectra III-V and VII have no MgO component, which would otherwise show the band gap onset at 7.8 eV - see the arrow. During these EELS measurements, the 1 nm<sup>2</sup> electron beam was placed next to the Au NPs, just off the MgO (Figure 3c), so indeed no signal from MgO is expected in these cases. In contrast to the absorption spectra in Figure 2a measured under far-field conditions, there is no obvious peak in the EELS spectrum for pure MgO at positions I, II and VI, as shown in Figure 3c. This might imply that the defect states in the single MgO NP are not uniformly distributed, or degrade too fast under electron irradiation to be detectable in the EELS spectrum. The onset of the MgO internal band gap at 7.8 eV, on the other hand, is clearly visible.

Interestingly, the EELS spectrum of MgO-Au nanocomposites shows strong peaks at 1.37 and 1.62 eV and weaker, broader peaks in the range ~1.8-2.5 eV. The EELS maps in Figure 3d show that the signal from the low-energy peaks is localized at large or touching Au NPs. These elongated volumes of Au would allow longitudinal plasmon modes to be established, which will not be possible in individual spherical Au NPs. Such longitudinal modes are occurring locally with oscillation frequencies—and hence energy values—strongly dependent on the exact size and shape of the elongated Au volume.<sup>[32]</sup> The high-energy peaks around 2.5 eV occur in all Au NPs and are typical transverse (short-distance, high-frequency) oscillations, the spectral amplitude of which depends on the number of electrons involved in the oscillations, and therefore, on the size of the Au NPs. High-energy peaks in the range 1.8–2.5 eV were also seen on more measured Au NPs than shown here, and the range for

these near-field individual resonance peaks matches the far-field collective UV-Vis peak at  $\sim 2.3$  eV (i.e. 530 nm) from Au in MgO-Au nanocomposites (Figure 2a). This makes sense: on the individual MgO-Au nanocomposite presented in Figure 3, a few strong longitudinal modes occur on elongated and touching particles, but on other MgO-Au nanocomposites, their length will be different, giving peaks at different energies. The high-energy modes from the non-touching Au NPs on the other hand, always occur in the range 1.8-2.5 eV on all MgO-Au nanocomposite, so in a collection of millions of these structures (UV-Vis experiments), the high-energy peaks add up and become dominant, while the low-energy peaks average out.

### 2.3. Stable H<sub>2</sub> Production from MgO-Au Nanocomposites

Subsequently, we performed a study of the photocatalytic activity for hydrogen production using either pure MgO NPs or MgO-Au nanocomposites with different Au NPs loadings, in the presence of methanol that resembles organic contaminants in wastewater (see Experimental Section for details). The obtained H<sub>2</sub> production results are presented in **Figure 4**. It is encouraging that the defect states of pure MgO NPs suspensions show photocatalytic activity in producing H<sub>2</sub> through water splitting. As shown in Figure 4a, the average H<sub>2</sub> production rate from pure MgO NPs is  $\sim 8.3 \mu\text{mol g}^{-1} \text{h}^{-1}$ . It is quite remarkable that the H<sub>2</sub> production rate from pure MgO NPs actually improves with time (Figure 4b), in contrast to many H<sub>2</sub> production systems with deteriorating performance over time, i.e. TiO<sub>2</sub>,<sup>[32]</sup> MoS<sub>2</sub>,<sup>[33]</sup> ZnO-CdS,<sup>[34]</sup> CuGaS<sub>2</sub><sup>[35]</sup> and ZnO-TiO<sub>2</sub>-CuO,<sup>[36]</sup> to name a few. As shown in Figure S8 (Supporting Information), we compared time-dependent H<sub>2</sub> production between MgO NPs and commercial TiO<sub>2</sub> (p25). From the results, we can see the stability of MgO is better than p25 as the H<sub>2</sub> production amount increases with time for MgO, while tends to saturate for p25. This is attributed to the large band gap and high chemical stability of MgO. The production of H<sub>2</sub> from pure MgO NPs indicates that photo-excited electrons in the surface defect energy



levels of MgO can be harvested to reduce protons ( $\text{H}^+$ ) from water for  $\text{H}_2$  production. At the same time, this result demonstrates that an oxygen plasma treatment is an effective method to remove the organic surfactants from nanomaterials synthesized via the oil-phase strategy. After the oxygen plasma treatment, MgO NPs have hydrophilic surfaces and become dispersible in water. This guarantees the direct contact between MgO NPs and water, enabling the photo-excited hot electrons to reach the protons for producing  $\text{H}_2$ . As magnesium is the fourth-most-abundant element on Earth (behind iron, oxygen and silicon), our simple scalable processing with ultra-stable performance could mean a much-improved economy for  $\text{H}_2$  production and waste treatment.

The presence of Au NPs on the surface of MgO NPs also has a dramatic effect on the efficiency of the photocatalytic  $\text{H}_2$  production. A series of measurements was done in which the amount of Au NPs in MgO-Au nanocomposites was varied from 13 wt% to 48 wt% (determined by ICP-AES). Figure 4a shows that the MgO-Au nanocomposites containing 23 wt% Au exhibited the highest  $\text{H}_2$  production rate of  $\sim 24.7 \mu\text{mol g}^{-1} \text{h}^{-1}$  compared to other Au NPs loadings, almost three times faster than the pure MgO NPs. Higher Au NPs loadings (e.g., 38 wt% and 48 wt%) lower the catalytic performance, even below that of pure MgO in the case of Au NPs loadings of 48 wt%. This can be explained by the fact that an increased coverage of the MgO surface reduces its direct light absorption, resulting in less photoexcited excitons. In addition, for these high-loaded MgO-Au nanocomposites, there is a higher chance that the Au NPs will be in mutual contact, yielding longitudinal surface plasmons at energies below  $\sim 1.8 \text{ eV}$ . When plasmons are excited below this energy, the electrons will not have enough energy to undergo interband transitions in the Au,<sup>[37]</sup> as discussed below, so no hot excitons will be excited that may contribute to proton reduction.

## 2.4. Density Functional Theory Calculations

Previous work has considered the nature of bulk defect states.<sup>[31]</sup> As we are studying MgO NPs, here we aim to rationalize the observed UV-Vis absorption and PL features by considering surface defects. We have used density functional theory calculations<sup>[38-40]</sup> with the PBE0 functional<sup>[41]</sup> on slabs of MgO, as described in the Supplement. Surface oxygen vacancies were the only defects that led to appreciable changes to the band gap region. In particular, notches exposing (110) surfaces that might be expected to yield states associated with 4-fold coordinated oxygen atoms did not lead to any gap states.

The calculated PBE0 density of states for a MgO slab with a surface oxygen vacancy is shown in **Figure 5**. The lowest energy unoccupied states are surface states in the absence of oxygen vacancies, which appear below the bulk conduction band minimum. Oxygen vacancies in the surface do not significantly alter this lowest energy unoccupied state. However, oxygen vacancies do introduce mid-gap defect (MGD) states, centered 3.1 eV above the top of the valence band. As indicated in Figure 5, these states correspond principally to electrons localized within the oxygen vacancy. The lowest energy unoccupied state ~2.9 eV above the MGD energy level is the pristine surface state aforementioned, which matches well to the PL emission center as observed (Figure 2b). Similar states that have been perturbed by the presence of the oxygen vacancy appear higher in energy as shown in Figure 5. Virtual states that are dominated by the oxygen vacancy, i.e. local excitations (LE) of the MGD states, first appear at the energy around 4.5 eV above the MGD state. Note that the spatial extent of the respective calculated projected densities indicate that there is significantly more overlap between the orbitals of the MGD states and these LE states around 4.5 eV than between the MGD states and lower energy surface states. This is consistent with the observed absorption peak at 4.6 eV from the MgO as shown in Figure 2a.

## 2.5. Insight into H<sub>2</sub> Production from MgO-Au Nanocomposites

The diagram in **Figure 6** proposes an explanation for the H<sub>2</sub> production of MgO NPs and its enhancement for MgO-Au nanocomposites.<sup>[10,42]</sup> Without Au NPs loading, MgO itself exhibits photocatalytic activity in H<sub>2</sub> production, as shown in Figure 4a. The surface electron-hole pairs will be generated when electrons transit from MGD to LE states after ionized/photoexcited via absorption of UV light at 270 nm/4.6 eV.<sup>[25,26,31]</sup> These excitonic electrons subsequently relax to lower energy levels, as indicated in Figure 6. The reduction of protons to H<sub>2</sub> may happen at the interface between the MgO surfaces<sup>[42,43]</sup> and water while matching the requirement that the energy level of the photoexcited electrons is higher than the proton reduction level (the H<sup>+</sup>/H<sub>2</sub> potential, Figure 6).

The band diagram for Au NPs in Figure 6 is derived from earlier work by Bond,<sup>[44]</sup> showing that the electrons nearly fill the 5d band and can be excited into the 6sp band via an interband transition of around 1.8 eV. Interestingly, this energy can be provided by surface plasmons, as long as the plasmon frequency is high enough to provide more than 1.8 eV of energy. And as discussed above, this is indeed the case for Au NPs that are small spheres or only slightly elongated. Large, elongated particles on the other hand, or nanoparticles that are in mutual contact, will generate longitudinal plasmons that resonate below 1.8 eV,<sup>[32,37,45]</sup> not providing enough energy to the electrons to undergo the interband transition. But with small enough, non-touching Au NPs, the oscillating electrons in the plasmon will have enough energy, and in each oscillation cycle, some of them will be excited into the 6sp band as hot electrons, while simultaneously creating hot holes. This relatively efficient excitation process results in fast electron damping in Au for plasmons that resonate at energies above ~1.8 eV.<sup>[45]</sup> Normally, the hot excitons thermalize in the Au,<sup>[46,47]</sup> but when the surrounding material provides nearby stable sites for the hot electrons, some of them will transfer out of the Au into these sites. This is the mechanism we propose here to explain the observed plasmon-stimulated photocatalysis: some of the hot electrons transfer into the MgO surface defect states where they are trapped and become available to reduce protons.

The lifetime of hot electrons in plasmon resonances is not much longer than the plasmon oscillation cycle itself, which is around 2 femtoseconds for the plasmons between 1.8 and 2.5 eV that we discuss here. Once they are trapped in defect states, the hot electron lifetimes are greatly enhanced.<sup>[46]</sup> A similar mechanism has been proposed for Au/TiO<sub>2</sub> heterostructures, where surface oxygen vacancies were shown to enhance photocatalytic H<sub>2</sub>O-splitting.<sup>[48]</sup> On the other hand, the local electric field from Au plasmons benefits the electron-hole separation,<sup>[49]</sup> thus further enhancing electron lifetimes. The increased lifetime of the hot electrons in MgO surface defects makes them more readily available to reduce protons, producing H<sub>2</sub>. As a result, protons in water have more effective access to electrons when Au NPs are present on MgO NPs, and the efficiency of the water splitting is greatly enhanced.

### 3. Conclusions

In summary, we have successfully performed a synergistic surface plasmon and defect states study on MgO-Au nanocomposites to enhance the proton photoreaction activity. The monodisperse, mesoporous and crystalline MgO-Au nanocomposites were synthesized via a facile, cheap and high-yielding green colloidal synthesis process. The MgO NPs exhibit robust proton photoreduction for H<sub>2</sub> production under UV excitation, which originates from MgO defect states as signified by theoretical calculations. Near-field measurements with monochromated EELS reveals the size/shape dependent plasmon resonance pattern of the gold nanoparticles that we used. Plasmon resonances in the energy range 1.8-2.5 eV contribute to the photoreduction enhancement, and we propose that this is the result of hot electron transfer from the Au into MgO surface defect states. The ultra-stable catalytic activity for H<sub>2</sub> production demonstrated here points to a new research avenue to develop a coordinated surface plasmon-defect technology for both energy conversion and decontamination applications within one green, sustainable and scalable photocatalysis system.

#### 4. Experimental Section

*Colloidal synthesis of MgO-Au nanocomposites:* The  $84 \pm 11$  nm sized MgO NPs were synthesized based on our previously reported method.<sup>[24]</sup> Then 16 mg of freshly prepared MgO NPs were added to a solution of OM (5 mL) with 8 mg of  $\text{AuCl}_3 \cdot \text{HCl} \cdot 4\text{H}_2\text{O}$  ( $\geq 47.8\%$ ). The solution was heated to 120 °C and kept at that temperature for 20 min. In this process, the color of the suspension changed from yellow to red. After cooling down to room temperature, the products were separated by adding an excess amount of ethanol and separated from the solution by centrifugation (10,000 rpm, 10 min), and then redispersed in cyclohexane.

*Measurement of photocatalytic hydrogen production:* In this study, pure MgO NPs and the based MgO-Au nanocomposites loaded with Au NPs of 13 wt%, 23 wt%, 38 wt% and 48 wt% (determined by ICP-AES) were tested for the photocatalytic water splitting to produce hydrogen. Note here that, before the photocatalytic experiments, all the MgO and MgO-Au powders were treated with the same oxygen plasma for 1 h to generate hydrophilic surfaces by removing the hydrophobic organic ligands. The photocatalytic hydrogen production experiments were performed in a 16 mL quartz flask under atmospheric pressure at room temperature. For each hydrogen production testing, MgO or MgO-Au powder (6 mg) was dispersed in deionized water (16 mL) by sonication for 45 min. Subsequently, 4 mL of methanol was added, which works as the sacrificial hole scavenger to mimic organics in wastewater. After that, the quartz flask was sealed with silicone rubber septum and then the reaction suspension in the flask was degassed with pure nitrogen gas for 30 min to remove the air inside, keeping the reaction suspension in an inert environment. After degassing, the quartz flask with reaction suspension was transferred and placed before the light source. A 150-W Xenon lamp (MAX-150, Asahi Spectra Co. Ltd., Japan) was used as a broadband light source covering the wavelength band between 250 and 1,000 nm, to trigger the photocatalytic reaction. The light illumination intensity on the flask was ca.  $250 \text{ mW cm}^{-2}$ , which was

measured by a Newport Power Meter (Model 1918-R) at the wavelength of 500 nm. The hydrogen was analyzed by a gas chromatography (Agilent 7890) with the installed gas valve system.

*Material characterization:* TEM images were acquired with a Hitachi HT-7700 transmission electron microscope operated at 100 kV. High-resolution TEM (HRTEM) micrographs were obtained with a Philips Tecnai F20 FEG-TEM operated at 200 kV. Monochromated EELS and scanning TEM images were measured with an FEI Titan TEM, operated at 80 kV using an electron probe size with a diameter of about 1 nm and an energy resolution of 120 meV, measured with a Gatan Tridiem ER EELS detector. Samples for TEM analysis were prepared by drying a drop of cyclohexane solution containing the nanocrystals on the surface of a carbon-coated copper grid. The X-ray diffraction (XRD) patterns were obtained using a Rigaku D/MAX-RB with monochromatized Cu K $\alpha$  radiation ( $\lambda=1.5418$  Å) and  $2\theta$  ranging from 30° to 80°. UV-Vis absorption spectra were measured on a Perkin-Elmer Lambda 35UV-vis spectrophotometer. Photoluminescence (PL) spectra were recorded on a Hitachi F-4600 spectrofluorophotometer at room temperature. The metal contents in the Au-loaded MgO nanocrystals were determined by a Leeman Labs Profile spec inductively coupled plasma atomic emission spectrometer (ICP-AES).

*Density functional theory:* 3D periodic projector augmented wave calculations were performed on slabs of MgO using the VASP code. The PBE GGA functional was used for geometry optimization before occupied and unoccupied states were examined via a single point calculation using the PBE0 hybrid functional at the relaxed PBE geometry. The thickness and vacuum distance of the slabs [with (100) faces] were selected by performing PBE calculations on a range of slabs varying these parameters and examining the  $\Gamma$ -point eigenenergies. Three layer slabs with 10 Å of vacuum between images gave a  $\Gamma$ -point spectrum not significantly different to thicker slabs with larger vacuum gaps. The final calculations were thus performed on five layer slabs with 10 Å of vacuum, with the extra

layers added so as to prevent significant interactions between surface defects and the other side of the slab. The lattice constant of the periodic directions was set to the bulk value (4.212 Å). 2×2 supercells of the surface unit cell (i.e. 8 formula units per slab layer) were used for investigating point defects with a 4×4×1  $\Gamma$ -centred reciprocal space grid. Only 1s electrons were frozen in the Mg and O potentials, and a 500 eV plane-wave cutoff was used throughout. Electronic states were visualized by examining the band-projected electron density in particular energy ranges spanning the density of states features of interest.

### Supporting Information

Supporting Information is available from the Wiley Online Library or from the author.

### Acknowledgements

We gratefully acknowledge financial support from the National Key R&D Program of China (2017YFA0208000), the China National Funds for Excellent Young Scientists (21522106), 111 Project (B18030), Singapore's National Research Foundation (Award No. NRF2016-NRF-ANR002), the ANU Futures Scheme (Q4601024), ANU Global Research Partnership Scheme (R468504649) and ActewAGL Endowment Fund (Q4601028). This work was undertaken with the assistance of resources and services from the National Computational Infrastructure (NCI), which is supported by the Australian Government.

### Conflict of Interest

The authors declare no conflict of interest.

Received: ((will be filled in by the editorial staff))  
Revised: ((will be filled in by the editorial staff))  
Published online: ((will be filled in by the editorial staff))

## References

- [1] C.-T. Yang, L. Wu, X. Liu, N. T. Tran, P. Bai, B. Liedberg, Y. Wang, B. Thierry, *Anal. Chem.* **2016**, 88, 11924-11930.
- [2] J. M. Bingham, J. N. Anker, L. E. Kreno, R. P. Van Duyne, *J. Am. Chem. Soc.* **2010**, 132, 17358-17359.
- [3] G. Lu, H. Li, C. Liusman, Z. Yin, S. Wu, H. Zhang, *Chem. Sci.* **2011**, 2, 1817-1821.
- [4] Y. Jiang, F. Meng, D. Qi, P. Cai, Z. Yin, F. Shao, H. Zhang, F. Boey, X. Chen, *Small* **2013**, 9, 2260-2265.
- [5] H. A. Atwater, A. Polman, *Nat. Mater.* **2010**, 9, 205.
- [6] J. Long, H. Chang, Q. Gu, J. Xu, L. Fan, S. Wang, Y. Zhou, W. Wei, L. Huang, X. Wang, P. Liu, W. Huang, *Energy Environ. Sci.* **2014**, 7, 973-977.
- [7] B. Wu, D. Liu, S. Mubeen, T. T. Chuong, M. Moskovits, G. D. Stucky, *J. Am. Chem. Soc.* **2016**, 138, 1114-1117.
- [8] Z. Yin, B. Chen, M. Bosman, X. Cao, J. Chen, B. Zheng, H. Zhang, *Small* **2014**, 10, 3537-3543.
- [9] X.-C. Ma, Y. Dai, L. Yu, B.-B. Huang, *Light-Sci. Appl.* **2016**, 5, e16017.
- [10] S. Linic, P. Christopher, D. B. Ingram, *Nat. Mater.* **2011**, 10, 911.
- [11] H. Eskandarloo, A. Kierulf, A. Abbaspourrad, *Nanoscale* **2017**, 9, 13850-13863.
- [12] B. Luo, D. Xu, D. Li, G. Wu, M. Wu, W. Shi, M. Chen, *ACS Appl. Mater. Interfaces* **2015**, 7, 17061-17069.
- [13] S. S. Boxi, S. Paria, *RSC Adv.* **2015**, 5, 37657-37668.
- [14] C. Hu, T. Peng, X. Hu, Y. Nie, X. Zhou, J. Qu, H. He, *J. Am. Chem. Soc.* **2010**, 132, 857-862.
- [15] H. A. Ghaly, A. S. El-Kalliny, T. A. Gad-Allah, N. E. A. Abd El-Sattar, E. R. Souaya, *RSC Adv.* **2017**, 7, 12726-12736.
- [16] J. Lin, J. P. B. Mueller, Q. Wang, G. Yuan, N. Antoniou, X.-C. Yuan, F. Capasso, *Science* **2013**, 340, 331-334.
- [17] H. Memmi, O. Benson, S. Sadofev, S. Kalusniak, *Phys. Rev. Lett.* **2017**, 118, 126802.
- [18] B. Lee, W. Liu, C. H. Naylor, J. Park, S. C. Malek, J. S. Berger, A. T. C. Johnson, R. Agarwal, *Nano Lett.* **2017**, 17, 4541-4547.
- [19] R. Chikkaraddy, B. de Nijs, F. Benz, S. J. Barrow, O. A. Scherman, E. Rosta, A. Demetriadou, P. Fox, O. Hess, J. J. Baumberg, *Nature* **2016**, 535, 127.
- [20] S. F. Tan, L. Wu, J. K. W. Yang, P. Bai, M. Bosman, C. A. Nijhuis, *Science* **2014**, 343, 1496-1499.



- [21] H. Li, Z. Bian, J. Zhu, Y. Huo, H. Li, Y. Lu, *J. Am. Chem. Soc.* **2007**, *129*, 4538-4539.
- [22] Y. Ben-Shahar, F. Scotognella, I. Kriegel, L. Moretti, G. Cerullo, E. Rabani, U. Banin, *Nat. Commun.* **2016**, *7*, 10413.
- [23] X.-L. Yin, J. Liu, W.-J. Jiang, X. Zhang, J.-S. Hu, L.-J. Wan, *Chem. Commun.* **2015**, *51*, 13842-13845.
- [24] Z. Liu, Z. Yin, C. Cox, M. Bosman, X. Qian, N. Li, H. Zhao, Y. Du, J. Li, D. G. Nocera, *Sci. Adv.* **2016**, *2*, e1501425.
- [25] S. Stankic, M. Sterrer, P. Hofmann, J. Bernardi, O. Diwald, E. Knözinger, *Nano Lett.* **2005**, *5*, 1889-1893.
- [26] M. Sterrer, T. Berger, O. Diwald, E. Knözinger, *J. Am. Chem. Soc.* **2003**, *125*, 195-199.
- [27] R. C. Whited, W. C. Walker, *Phys. Rev. Lett.* **1969**, *22*, 1428-1430.
- [28] M. Klaua, D. Ullmann, J. Barthel, W. Wulfhekel, J. Kirschner, R. Urban, T. L. Monchesky, A. Enders, J. F. Cochran, B. Heinrich, *Phys. Rev. B* **2001**, *64*, 134411.
- [29] G. H. Rosenblatt, M. W. Rowe, G. P. Williams, R. T. Williams, Y. Chen, *Phys. Rev. B* **1989**, *39*, 10309-10318.
- [30] E. Feldbach, R. Jaaniso, M. Kodu, V. P. Denks, A. Kasikov, P. Liblik, A. Maaros, H. Mändar, M. Kirm, *J. Mater. Sci.-Mater. Electron.* **2009**, *20*, 321-325.
- [31] P. Rinke, A. Schleife, E. Kioupakis, A. Janotti, C. Rödl, F. Bechstedt, M. Scheffler, C. G. Van de Walle, *Phys. Rev. Lett.* **2012**, *108*, 126404.
- [32] V. Myroshnychenko, J. Rodriguez-Fernandez, I. Pastoriza-Santos, A. M. Funston, C. Novo, P. Mulvaney, L. M. Liz-Marzan, F. J. Garcia de Abajo, *Chem. Soc. Rev.* **2008**, *37*, 1792-1805.
- [33] X. Hai, W. Zhou, K. Chang, H. Pang, H. Liu, L. Shi, F. Ichihara, J. Ye, *J. Mater. Chem. A* **2017**, *5*, 8591-8598.
- [34] H. Zhao, Y. Dong, P. Jiang, G. Wang, H. Miao, R. Wu, L. Kong, J. Zhang, C. Zhang, *ACS Sustain. Chem. Eng.* **2015**, *3*, 969-977.
- [35] K. Iwashina, A. Iwase, Y. H. Ng, R. Amal, A. Kudo, *J. Am. Chem. Soc.* **2015**, *137*, 604-607.
- [36] Z. Yin, Z. Wang, Y. Du, X. Qi, Y. Huang, C. Xue, H. Zhang, *Adv. Mater.* **2012**, *24*, 5374-5378.
- [37] C. Sönnichsen, T. Franzl, T. Wilk, G. von Plessen, J. Feldmann, O. Wilson, P. Mulvaney, *Phys. Rev. Lett.* **2002**, *88*, 077402.
- [38] G. Kresse, J. Furthmüller, *Phys. Rev. B* **1996**, *54*, 11169-11186.
- [39] H. Jürgen, *J. Comput. Chem.* **2008**, *29*, 2044-2078.

- [40] G. Kresse, D. Joubert, *Phys. Rev. B* **1999**, *59*, 1758-1775.
- [41] J. P. Perdew, M. Ernzerhof, K. Burke, *J. Chem. Phys.* **1996**, *105*, 9982-9985.
- [42] C. G. Zoski, *Handbook of electrochemistry*, Elsevier, **2006**.
- [43] Z. Ding, L. Yan, Z. Li, W. Ma, G. Lu, S. Meng, *Phys. Rev. Mater.* **2017**, *1*, 045404.
- [44] G. C. Bond, *Faraday Discuss.* **2011**, *152*, 277-291.
- [45] M. Bosman, E. Ye, S. F. Tan, C. A. Nijhuis, J. K. W. Yang, R. Marty, A. Mlayah, A. Arbouet, C. Girard, M.-Y. Han, *Sci. Rep.* **2013**, *3*, 1312.
- [46] Y. Zhang, S. He, W. Guo, Y. Hu, J. Huang, J. R. Mulcahy, W. D. Wei, *Chem. Rev.* **2018**, *118*, 2927-2954.
- [47] L. Yan, F. Wang, S. Meng, *ACS Nano* **2016**, *10*, 5452-5458.
- [48] J. B. Priebe, J. Radnik, A. J. J. Lennox, M.-M. Pohl, M. Karnahl, D. Hollmann, K. Grabow, U. Bentrup, H. Junge, M. Beller, A. Brückner, *ACS Catal.* **2015**, *5*, 2137-2148.
- [49] J. Schneider, M. Matsuoka, M. Takeuchi, J. Zhang, Y. Horiuchi, M. Anpo, D. W. Bahnemann, *Chem. Rev.* **2014**, *114*, 9919-9986.

## FIGURES

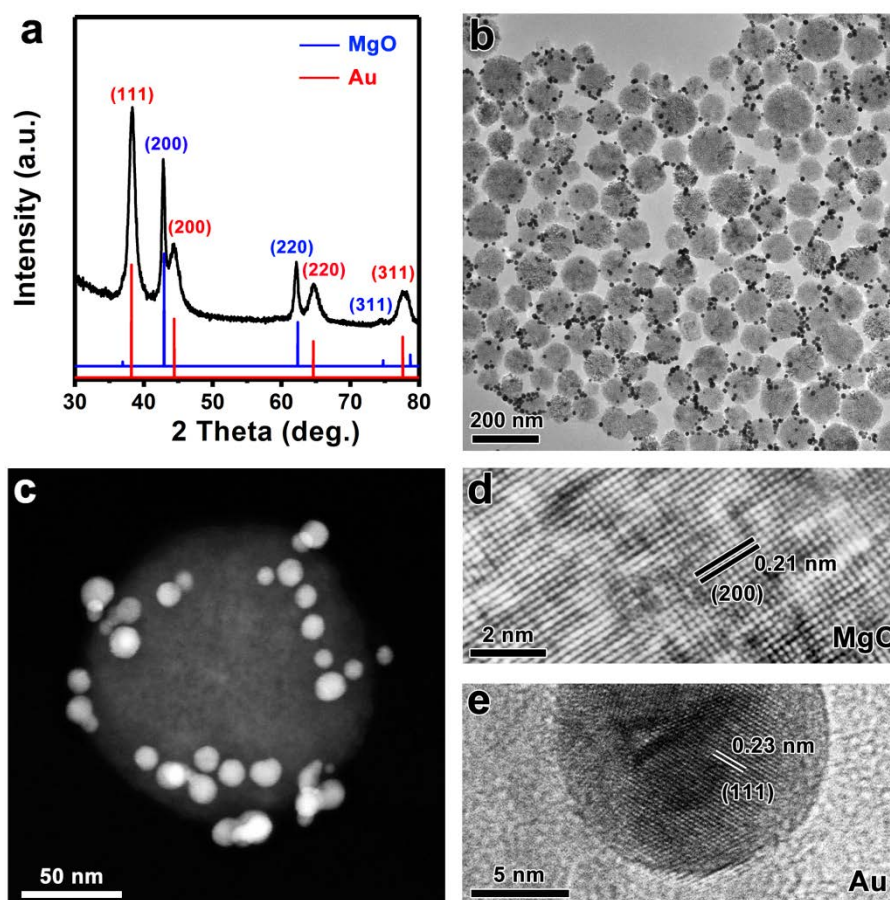


**Figure 1.** (a) XRD pattern of MgO-Au nanocomposites. (b) TEM and (c) HAADF-STEM images of Au-loaded MgO NPs. HRTEM images of the (d) MgO and (e) Au acquired from the MgO-Au nanocomposites.

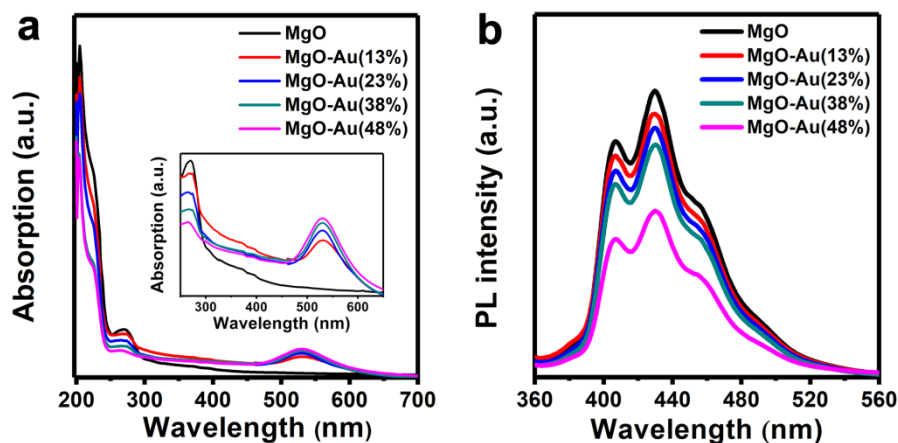


**Figure 2.** (a) Room temperature UV-Vis absorption and (b) PL ( $\lambda_{ex} = 340$  nm) spectra of pure MgO NPs and MgO-Au nanocomposites. The concentration of all samples was kept at  $0.1 \text{ mg mL}^{-1}$  dispersed in cyclohexane. The inset in (a) shows a magnification of the plots within the wavelength range of 250–650 nm.

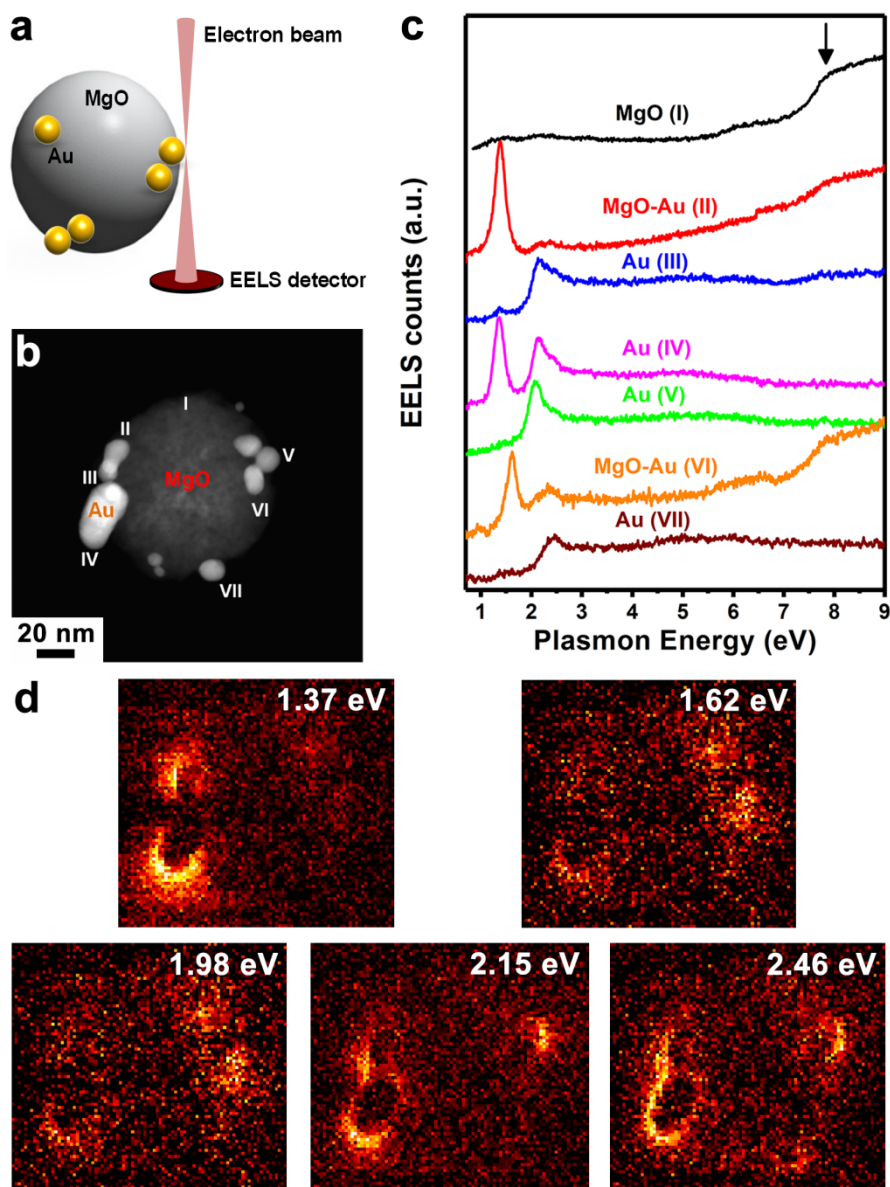


**Figure 3.** (a) Schematic experimental configuration of the plasmon measurements using monochromated EELS: a focused  $\sim 1$  nm electron beam excites the surface plasmons in Au NPs on MgO, resulting in energy losses that are measured by the EELS detector. (b) STEM image of a MgO-Au nanocomposite; the Au NPs appear bright on the grey, spherical MgO nanocrystal. (c) EELS spectra obtained from different locations, as indicated by Roman numerals in the STEM image. MgO (I), MgO-Au (II, VI), and Au (III, IV, V and VII). (d) Monochromated EELS maps for the MgO-Au nanocomposite shown in (b) at the five plasmon resonance energies of Au, showing the spatial distribution of the modes. For thick parts of the MgO, the EELS signal is low, as most of the electrons are elastically scattered and do not reach the EELS detector.

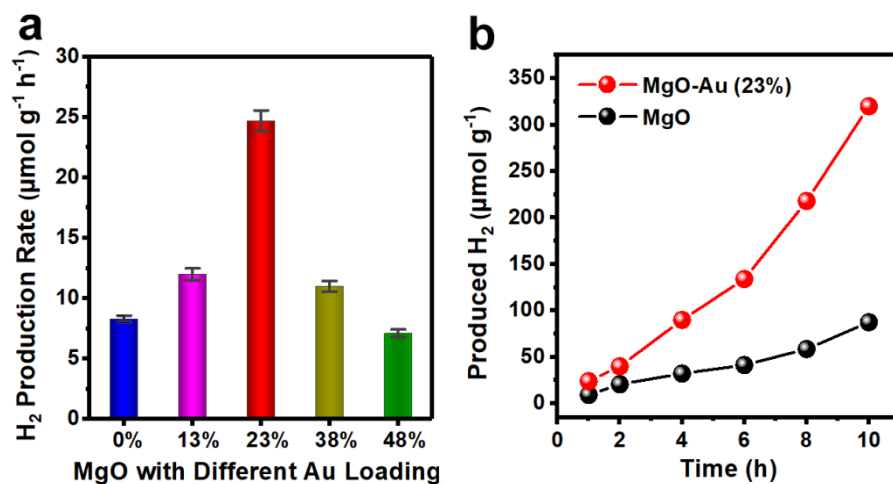


**Figure 4.** (a)  $H_2$  production rate for MgO-Au nanocomposites with different weight loading of gold based on  $84 \pm 11$  nm sized MgO NPs; and (d) average production of  $H_2$  versus the illumination time from MgO-Au nanocomposites with 23 wt% Au versus pure MgO NPs as the control.

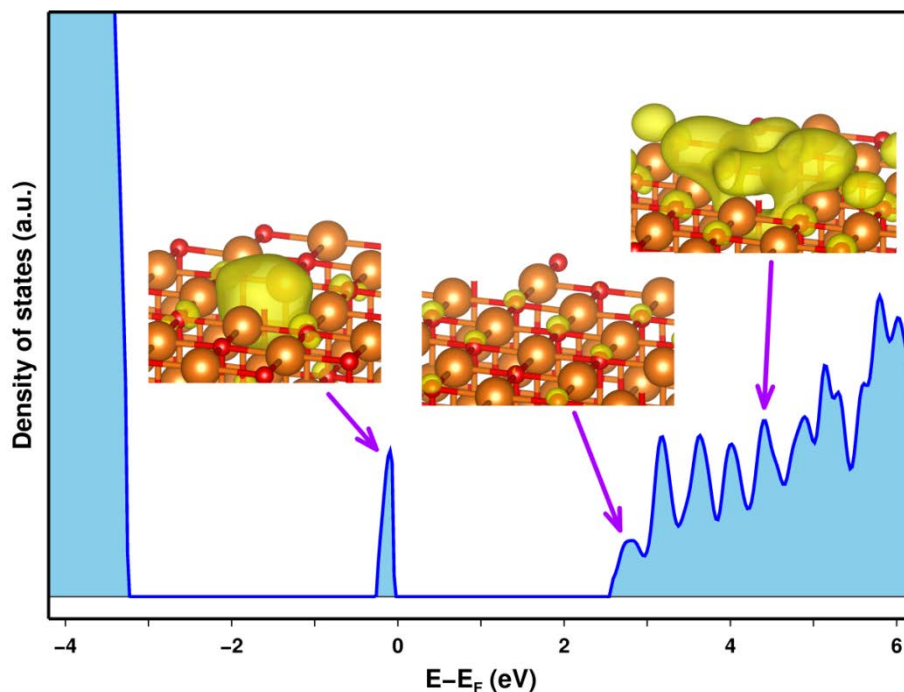


**Figure 5.** Calculated density of states for MgO slab with a surface oxygen vacancy. The energy axis is shifted to be relative to the calculated Fermi energy ( $E_F$ ). Isosurfaces of projected electron densities are shown for energies spanning the indicated features. Near  $E - E_F = 0$ , mid-gap defect states can be seen, while at  $E - E_F = 4.5$  eV, locally excited states are observed. Mg ions shown as larger orange balls, O ions shown as smaller red balls. The surface oxygen ion removed to make the vacancy defect would be located in the centre of the surfaces shown in the left and right inset images, in the vicinity of the associated projected electron density that is shown; the central inset shows a different part of the surface without an oxygen defect.

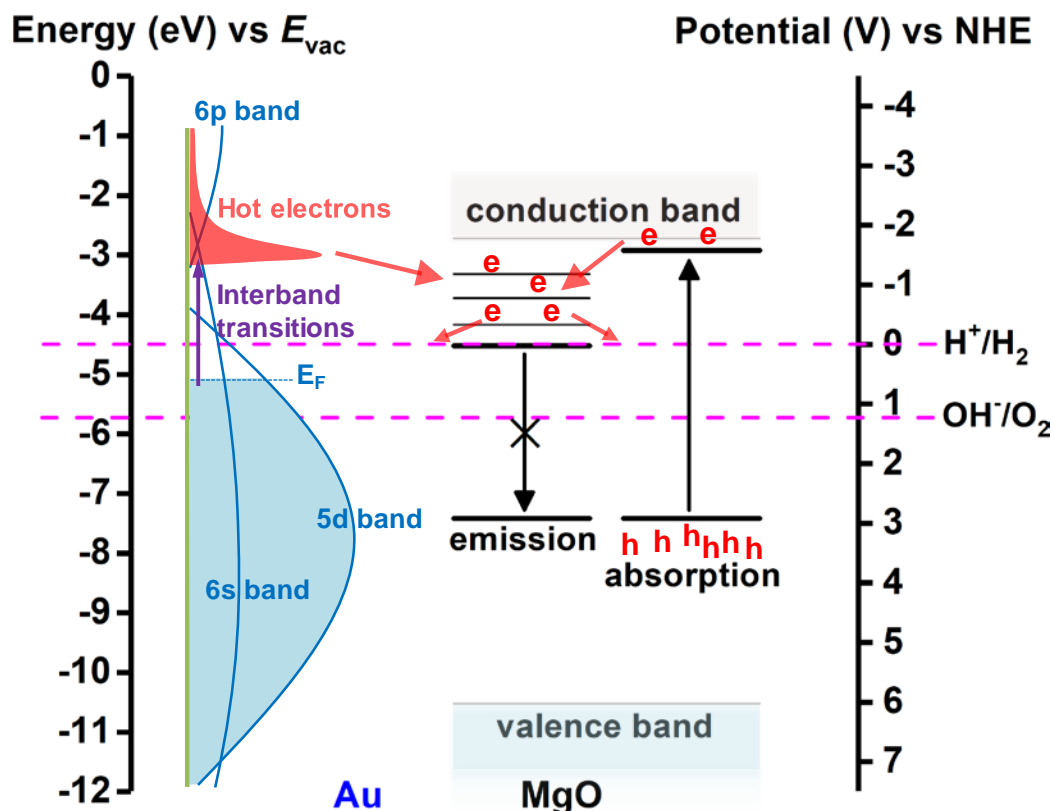


**Figure 6.** The band structure for Au NPs is based on work by Bond,<sup>[44]</sup> showing that the electrons can undergo an interband transition (purple arrow) from the 5d band to the 6sp bands, exciting hot electrons. Some of these hot electrons subsequently transfer to defect states in nearby MgO. Based on ultraviolet photoelectron spectroscopy (UPS) results,<sup>[24]</sup> the valence band maximum for MgO is around -10.5 eV. Combined with the 7.8 eV band gap of MgO, we infer a conduction band minimum, of -2.7 with respect to the vacuum energy level ( $E_{\text{vac}} = 0$ ). The energy levels in the emission region are taken from the calculated surface/defect states in Figure 5, where the lowest energy level is 2.9 eV above the mid-gap energy level (-6.6 eV), consistent with the dominant emission peak center at 2.9 eV (430 nm) from the PL results of Figure 2b. In the absorption region, the locally-excited state, 4.5 eV above the mid-gap level, also refers to the calculated result in Figure 5. The plasmon- and photoexcited electrons present in the MgO defect states reduce protons in water and contribute to the production of  $\text{H}_2$ . For comparison, the energy scale vs  $E_{\text{vac}}$  is plotted along with the scale that indicated the redox potential vs the normal hydrogen electrode (NHE).<sup>[10,42]</sup> The redox potentials for the water-splitting half-reactions ( $\text{H}^+/\text{H}_2$  and  $\text{OH}^-/\text{O}_2$ ) versus the NHE are indicated by dashed pink lines. The work function of gold is set at -5.1 eV.



A **plasmonic defect nanosystem** is successfully established via a MgO-Au nanocomposite by a facile, non-toxic and inexpensive method, in which mesoporous MgO nanoparticles possess stable surface defect states, giving stable photoactivity in  $\text{H}_2$  generation via water splitting. With the introduction of plasmonic gold nanoparticles, both the photoactivity and stability of MgO defect states are significantly enhanced.

### Keyword

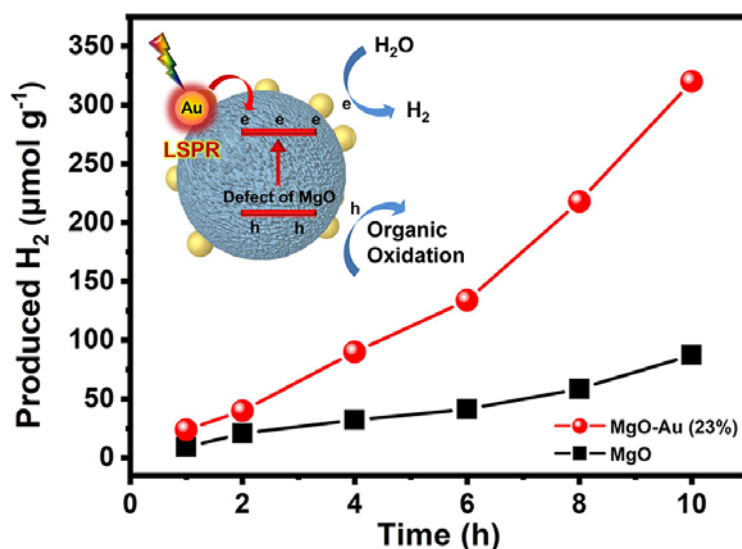
Plasmonic defect nanosystems, oxygen vacancies, surface plasmon, co-enhancement of photoactivity and stability

Z. Q. Liu, Z. Y. Lu, M. Bosman, N. Li, T. J. Frankcombe, \* G. H. Jia, A. Tricoli, Y. Liu, Y. P. Du, \* and Z. Y. Yin\*

### Title

Photoactivity and Stability Co-enhancement: When Localized Plasmons Meet Surface Defects

ToC figure



## Supporting Information

**Photoactivity and Stability Co-enhancement: When Localized Plasmons Meet Oxygen Vacancies in MgO**

Zhengqing Liu,<sup>+</sup> Ziyang Lu,<sup>+</sup> Michel Bosman, Na Li, Terry J. Frankcombe,<sup>\*</sup> Guohua Jia, A. Tricoli, Y. Liu, Yaping Du,<sup>\*</sup> and Zongyou Yin<sup>\*</sup>

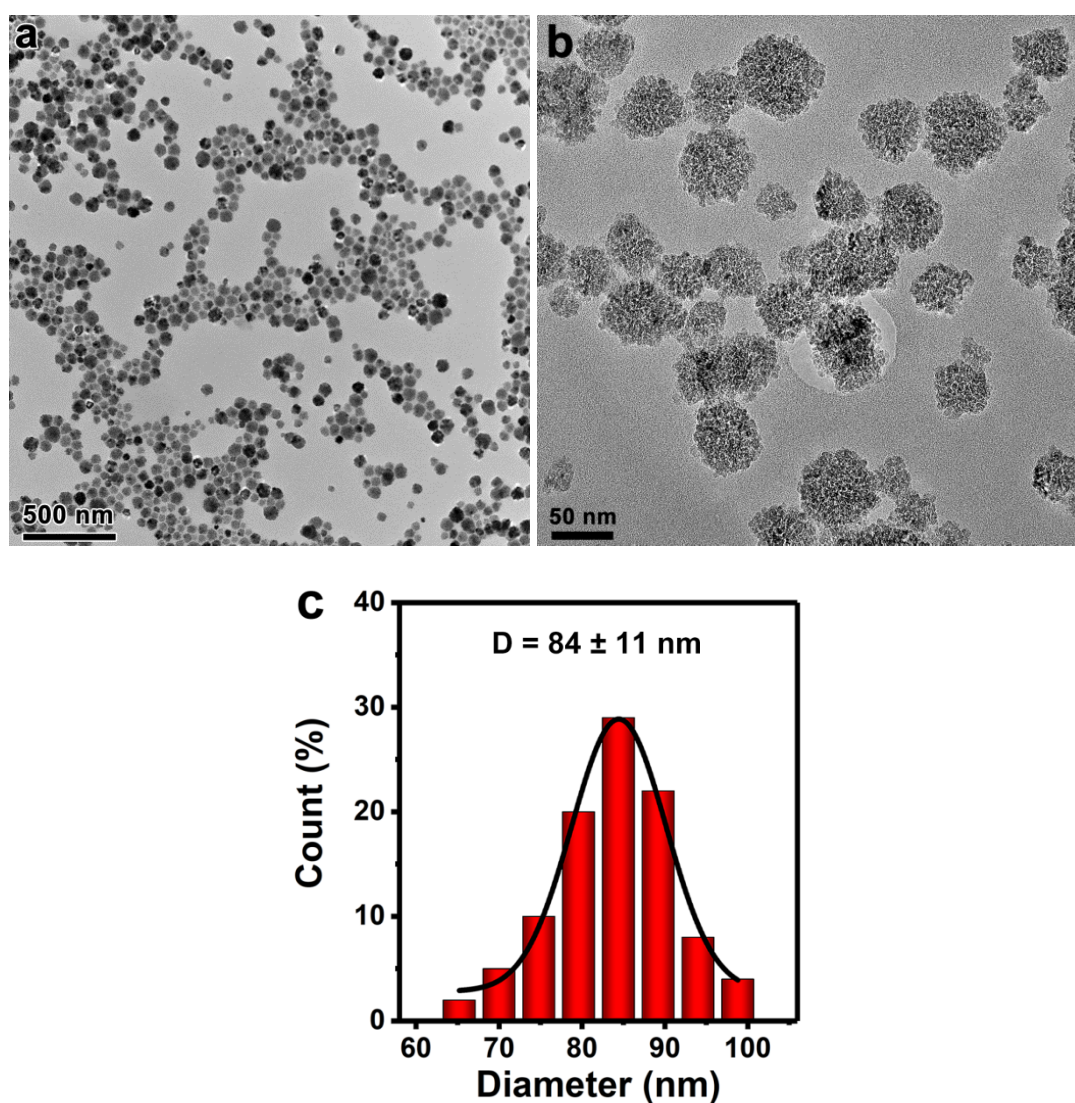


**Figure S1.** (a,b) TEM images of synthesized MgO NPs with mesoporous morphology. (c) Statistical analysis of the sizes of MgO NPs measured by TEM image of (a), in which 84 nm is the mean size and 11 nm is the standard deviation.

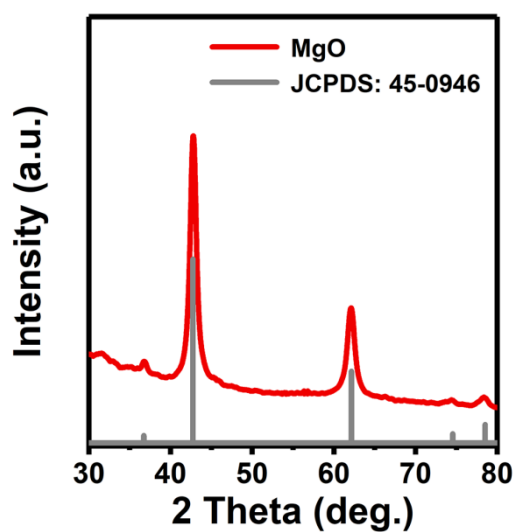


**Figure S2.** XRD pattern of the synthesized pure MgO NPs with a pure cubic phase (space group: Fm-3m, JCPDS: 45-0946).

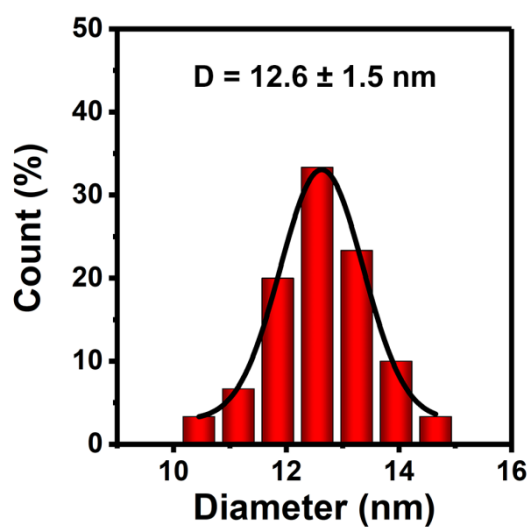


**Figure S3.** Statistical analysis of the sizes of Au NPs from MgO-Au nanocomposites measured by TEM image of Fig. 1b, in which 12.6 nm is the mean size and 1.5 nm is the standard deviation.

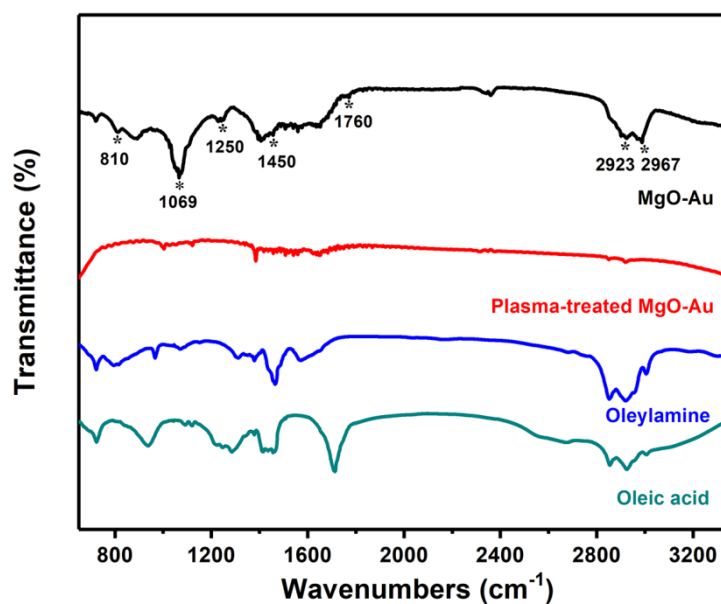


**Figure S4.** FTIR spectra (Nicolet 6700) of oleylamine, oleic acid, as-prepared MgO-Au nanocomposites and plasma-treated MgO-Au nanocomposites. The presence of acyclic C-H stretching at  $2967\text{ cm}^{-1}$  and  $2923\text{ cm}^{-1}$  indicate the co-existence of oleic acid and oleylamine. The peaks at  $1760\text{ cm}^{-1}$  and  $1450\text{ cm}^{-1}$  are assigned to C=O stretch and carboxylate ( $\text{COO}^-$ ) stretch, implying the  $\text{COO}^-$  ligand exists on the surface of the MgO-Au nanocomposites. Additionally, the three peaks at  $1250$ ,  $1069$  and  $810\text{ cm}^{-1}$  in the IR spectrum of MgO-Au nanocomposites were indexed to C-N stretch of oleylamine, respectively. Based on the FTIR analysis of MgO-Au nanocomposites, it is confirmed that these MgO-Au nanocomposites are coated by two kinds of organic molecules, oleylamine and oleic acid. Note here, after oxygen plasma treatment, the intensity of characteristic peaks of oleic acid and oleylamine obviously decreased, indicating a successful removal of organic capping ligands from the surface of MgO-Au nanocomposites.

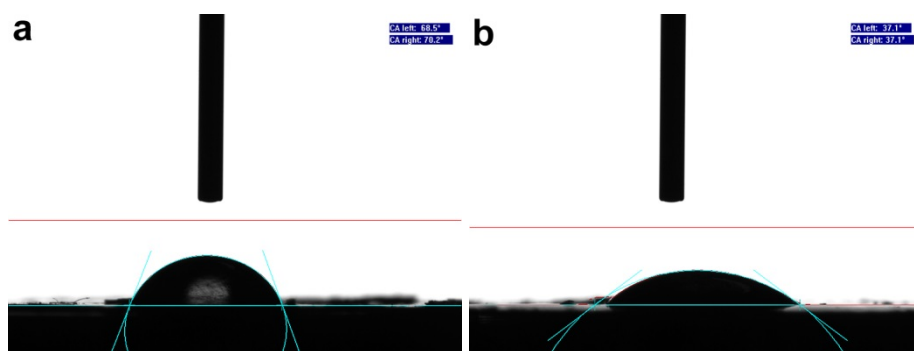


**Figure S5.** The contact angle of (a) pristine MgO NPs and (b) oxygen plasma treated MgO NPs. The contact angle of pristine MgO NPs and oxygen plasma treated MgO NPs are  $69.4^\circ$  and  $37.1^\circ$ , respectively. By comparison, we found that the contact angle of oxygen plasma treated MgO NPs is significantly decreased, indicating that the oxygen plasma treatment is very efficient in cleaning the nanomaterial surfaces by removing the organic capping ligands.

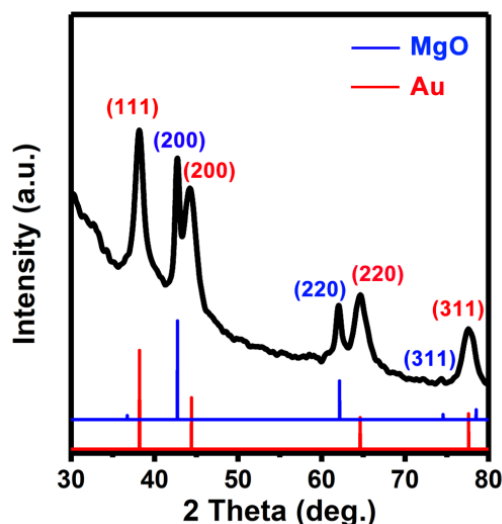


**Figure S6.** XRD pattern of the MgO-Au nanocomposites after plasma treatment.

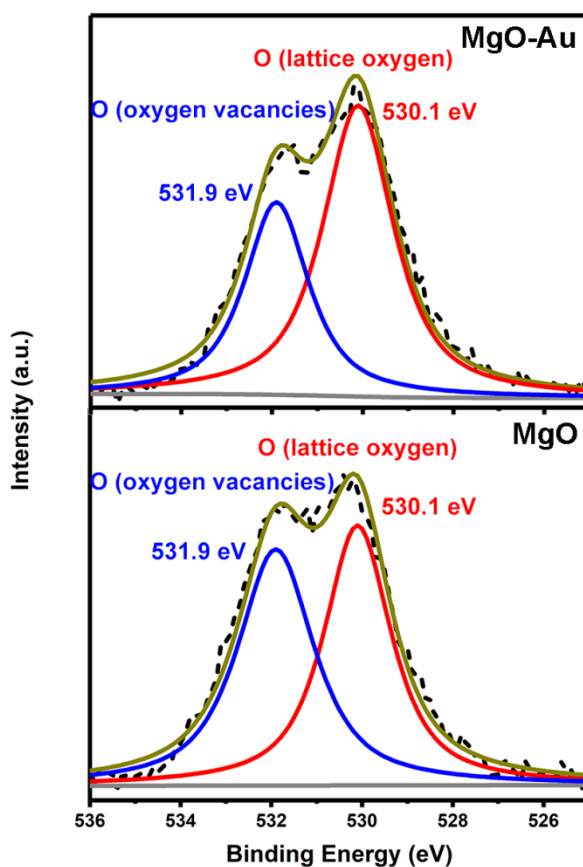


**Figure S7.** XPS spectra of O 1s for MgO and MgO-Au nanocomposites after plasma treatment. It is observed that the O 1s spectra of MgO and MgO-Au nanocomposites showed two peaks. The major peak located at around 530.1 eV could be associated with the lattice oxygen in MgO, which is the characteristic of chemical bonding between metal and oxygen atom, while the smaller peak located at around 531.9 eV was ascribed to the surface oxygen vacancies.<sup>[S1-S3]</sup> Therefore, the XPS results show that oxygen vacancies are present in the as-prepared MgO and MgO-Au samples.

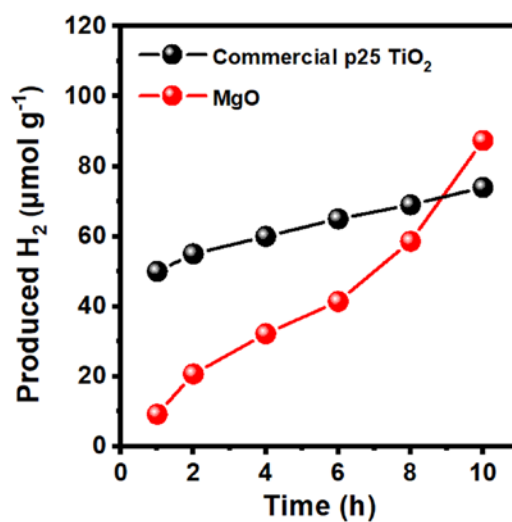


**Figure S8.** Comparison of  $\text{H}_2$  production between MgO NPs in this work and commercial  $\text{TiO}_2$  (p25).

#### Reference

- [S1] J. S. Corneille, J. W. He, D. W. Goodman, *Surf. Sci.* **1994**, *306*, 269-278.
- [S2] G. Yang, D. Gao, J. Zhang, J. Zhang, Z. Shi, D. Xue, *J. Phys. Chem. C* **2011**, *115*, 16814-16818.
- [S3] D. Mishra, B. P. Mandal, R. Mukherjee, R. Naik, G. Lawes, B. Nadgorny, *Appl. Phys. Lett.* **2013**, *102*, 182404.